Polym. Bull. (2015) 72:2757–2782
DOI 10.1007/s00289-015-1434-0

ORIGINAL PAPER

Isotactic polypropylene (PP) modified by ABS and $CaCO_3$ nanoparticles: effect of composition and compatibilization on the phase morphology, mechanical properties and fracture behavior

Omid Momen[1] · Majid Mehrabi-Mazidi[2] · Neda Jahangiri[1]

Received: 3 March 2014 / Revised: 25 April 2015 / Accepted: 7 June 2015 /
Published online: 17 June 2015

Abstract Attempt was made to improve the properties of isotactic polypropylene (iPP) by simultaneous incorporation of ABS and $CaCO_3$ nanoparticles. The goal was to achieve a balanced toughness and stiffness by the development of ternary PP/ABS/$CaCO_3$ nanocomposite. The effects of compatibilization and composition on the phase morphology, mechanical properties and deformation behavior under impact loadings were systematically studied. The phase structure and mechanical properties of binary PP/ABS and PP/$CaCO_3$ systems was also investigated in detail to clarify the contribution of individual ABS and $CaCO_3$ components in the macroscopic response of ternary hybrid. It was found that the ABS could effectively toughen the PP matrix by the suitable compatibilization. Moreover, the $CaCO_3$ nanoparticles alone serve as stiffener and toughener in the material. Accordingly, the impact toughness of ternary PP/ABS/$CaCO_3$ nanocomposites was larger than those of compatibilized PP/ABS blend and PP/$CaCO_3$ system and, therefore, much higher than that of unmodified iPP. The mechanical properties and toughening mechanisms of different binary and ternary samples were rationalized by fractographic analysis. In the case of Izod impact-fractured samples, the characteristics of fractured surfaces were closely examined at the crack initiation and propagation stages of the impact fracture process.

Keywords Morphology · Mechanical properties · Compatibilization · Impact toughness · Fractography

✉ Majid Mehrabi-Mazidi
ma_mehrabi84@yahoo.com; m_mehrabi@sut.ac.ir

[1] Department of Polymer Engineering, Shiraz Branch, Islamic Azad University, Shiraz, Iran

[2] Polymer Engineering Department, Institute of Polymeric Materials, Sahand University of Technology, Sahand New Town, Tabriz, Iran

Introduction

Isotactic polypropylene (iPP) is the most widely used commodity thermoplastic with very large consumption because of its attractive properties such as low cost, good mechanical properties and easy processing [1–3]. However, its application as a structural material is restricted due to its poor impact resistance, especially at low temperatures. It is well known that the impact toughness of PP can greatly be improved by the addition of elastomers such as ethylene–propylene rubber (EPR), ethylene–propylene diene monomer (EPDM) and styrene–ethylene butylene–styrene (SEBS) triblock copolymer as a secondary discrete phase. The improved toughness upon the addition of rubbery phase is obtained at the cost of a reduction in stiffness, yield stress, ultimate strength and heat resistance. These properties generally decrease with rubber content. On the other hand, the introduction of inorganic fillers into PP overcomes these problems but most often reduces the fracture toughness [4–7]. Therefore, issues concerned with the simultaneous reinforcing and toughening of PP have attracted considerable attention. The incorporation of both rigid reinforcement and elastomeric phases into PP leads to the formation of ternary or hybrid composites, which have attracted much attention due to their potentiality in achieving both high stiffness and high toughness [6, 8–15]. In these heterogeneous systems, the macroscopic performance of the material is strongly dependent on the microstructure which, in turn, is controlled by the concentration of components, mutual interaction between the components and the processing conditions as well [6, 10–12, 16, 17]. Two main phase morphologies have been reported in the literature for the PP/elastomer/filler ternary systems [11, 18–20]; one is morphology that the elastomer and filler particles are dispersed independently in the PP matrix. Another has core–shell-type particles consisting of a filler particle core and an elastomer shell. The formation of these morphologies is reported to be strongly dependent on the interactions between the elastomer and filler. When no functional group is introduced into the elastomer, the elastomer and the filler particles are dispersed separately in the PP matrix because there is no interaction between the elastomer and the filler particles. On the other hand, when the functionalized elastomer is used to enhance the interaction between the elastomer and filler, the aforementioned core–shell structure should be formed.

There is a number of studies in the literature that dealt with the phase morphology and mechanical properties of PP/elastomer/nano-$CaCO_3$ nanocomposites [9, 11–15, 21]. Ma et al. [9] studied the phase structure and mechanical properties of PP/ethylene–octene rubber (POE)/nano-$CaCO_3$ composites. They found that both the segregated dispersion state and core–shell structure, in which ethylene–octene copolymer (POE) acted as the shell part encapsulating calcium carbonate nanoparticles (nano-$CaCO_3$), in the PP/POE/$CaCO_3$ ternary composites could significantly increase the notched impact toughness as compared with PP/POE blend or neat PP. Hikasa et al. [11] investigated morphology and impact behavior of PP/SEBS/nano-$CaCO_3$ composites. They used two kinds of SEBS triblock copolymer in their work; SEBS and carboxylated SEBS (C-SEBS). They demonstrated that the composite with SEBS showed a morphology in which SEBS domains and $CaCO_3$ particles were independently dispersed in the PP matrix, while the composite with C-SEBS showed a

morphology in which $CaCO_3$ particles were encapsulated by C-SEBS. For the PP/EPDM/nano-$CaCO_3$ ternary nanocomposite, Gong et al. [13, 14] described the effect of mixing sate on the morphology and mechanical properties. Due to the cavitation initiated by the debonding and the fibrillation present at interface as a result of well-dispersed nano-$CaCO_3$ particles, the impact strength was pronouncedly enhanced. It is important to note that in all of the systems mentioned above, the rubbery phase has been compatible with the PP matrix and thus a good interfacial adhesion was assured between the rubbery phase and the matrix, which is a main prerequisite for obtaining a suitable rubber toughening effect.

The present work was aimed to study the influence of compatibilization and composition on the morphology, mechanical properties and deformation behavior of ternary system based on PP modified with soft ABS and rigid nano-$CaCO_3$ particles. To our best knowledge, the toughening efficiency of ABS rubber particles for isotactic PP has not been studied before. It should be noted that the ABS particles are commercially used as a toughening agent for styrenic matrices, most frequently poly(styrene-*co*-acrylonitrile) copolymer. The rubbery nature of ABS along with its particle size distribution (ranging from 0.1 to 1 μm) which is close to the optimum particle size for effective toughening in semicrystalline matrices (such as iPP) was the main reason for the evaluation of toughening capability of ABS particles for the iPP matrix in the present research work. Since ABS rubber particles are not compatible with PP, the PP-*g*-MA was used as compatibilizer. The goal was to simultaneously enhance the toughness and stiffness of iPP by the development of PP/ABS/$CaCO_3$ ternary hybrid. The phase structure and mechanical properties of PP/ABS and PP/nano-$CaCO_3$ binary systems were also examined in detail to separately evaluate the functionality of individual ABS and nano-$CaCO_3$ components in the PP matrix and to distinguish their respective influences on the mechanical performance of ternary PP/ABS/nano-$CaCO_3$ nanocomposite. In the case of PP/ABS/$CaCO_3$ ternary systems, the attention was paid at a fixed composition. Detailed investigations into the properties of ternary systems at a wider range of ABS and $CaCO_3$ concentrations will be presented in the papers to be published later.

Experimental

Materials

All the materials used in this work were supplied from commercial sources. Isotactic polypropylene (iPP) (MFI = 6 g/10 min, 2.16 kg at 230 °C) and polybutadiene-*g*-poly(styrene-*co*-acrylonitrile) (denoted as ABS in the present work) impact modifier with the particle size ranging from 0.1 to 1 μm were, respectively, purchased from Jam and Ghaed Basir Petrochemical Companies, Iran. The ABS rubbery phase had a core–shell microstructure in which the polybutadiene core was chemically grafted by a shell of styrene–acrylonitrile (SAN) copolymer with the PB/SAN ratio of about 60:40 by weight. The maleic anhydride-grafted PP (PP-*g*-MA) (polybond 3150) was supplied by Crompton Corp., with the maleic anhydride content of about 0.5 wt%. The calcium carbonate ($CaCO_3$) nanoparticles with the

average particle size of 80 nm were obtained from Shiraishi Kogyo Kaisha Ltd, Japan. The nanoparticles were surface coated by fatty acids by the manufacturer.

Sample preparation

The melt mixing of all samples was carried out in an internal mixer (Brabender Plasticorder) operated at 190 °C and rotor speed of 80 rpm for 8 min. Before mixing, the $CaCO_3$ nanoparticles were dried in an oven at 120 °C for 2 h and then cooled down to room temperature. The composition of binary and ternary systems prepared in this study is listed in Table 1. Samples for tensile (ISO 527) and notched Izod (ASTM D256) impact tests were compression molded by a hot press machine at 190 °C under 50 bar and cooled to ambient temperature by water with 15 ± 5 °C min^{-1} average cooling rate.

Mechanical properties

The tensile tests were conducted on a MTS10/M universal testing machine at a fixed crosshead speed of 5 mm/min at ambient temperature. At least four specimens were tested for each composition, and the resulting tensile properties were averaged. In addition to tensile tests, the response of the samples under the notched Izod impact

Table 1 The notation and composition of the binary and ternary systems studied in this work

Material (notation)	Composition (wt%)			
	PP	Nano-$CaCO_3$	ABS	PP-*g*-MA
PP	100	0	0	0
PP/nano-$CaCO_3$				
	99	1	0	0
	97	3	0	0
	95	5	0	0
	90	10	0	0
PP/ABS				
	95	0	5	0
	90	0	10	0
	80	0	20	0
	94	0	5	1
	89	0	10	1
	79	0	20	1
	92	0	5	3
	87	0	10	3
	77	0	20	3
	74	0	20	6
PP/ABS/nano-$CaCO_3$				
	75	5	20	0
	69	5	20	6

tests (GOTECH TCS 2000 pendulum impact tester) was also determined. The results of the impact strength are the average of at least five repetition obtained at room temperature.

Morphological observations

The morphological texture of the cryo-fractured samples was analyzed using a TESCAN FEG scanning electron microscopy (SEM) instrument, operated in high vacuum mode. Undeformed molded specimens were examined by cryo-fracturing to obtain a survey of filler dispersion. To study the effect of compatibilizer on the phase morphology, the ABS rubbery phase was etched by tetrahydrofuran (THF) at room temperature for 24 h. Then, the samples were dried in a vacuum oven overnight. Prior to SEM observations, all the samples were coated with a thin layer of gold and then the micrographs were taken with different magnifications.

Fracture surface analysis

To elucidate the role of different rigid and soft phases on the fracture behavior of the samples, and also to understand the micromechanisms of deformation related to the different systems, FEG-SEM micrographs were also taken from the tensile and impact-fractured specimens of different compositions. In the case of samples fractured under impact loadings, the micrographs were prepared at different regions on the fractured surface corresponding to the crack initiation and crack propagation stages of the fracture process.

Results and discussion

To clarify the effects of different ABS and nano-$CaCO_3$ phases on the mechanical and morphological properties of ternary systems, the functionality of individual phases in the PP matrix was investigated at first. The dispersion quality of nano-$CaCO_3$ particles in PP/$CaCO_3$ nanocomposites of various filler loadings is depicted in Fig. 1.

It is known that the dispersion of an inorganic filler in a thermoplastic is not an easy process. The problem is even more severe when using nanoparticles as filler, because the nanoparticles have a strong tendency to agglomerate. Therefore, homogeneous dispersion of nanofillers in the thermoplastic matrices is a difficult process [22]. From Fig. 1, it seems that a good dispersion of nanoparticles was obtained for nanocomposites of different filler contents prepared in this work, although very little number of small aggregates was formed in the nanocomposite with 10 wt% of $CaCO_3$ nanoparticles (Fig. 1b). A homogeneous dispersion of $CaCO_3$ nanoparticles in this study indicates that most of the particles were distributed within PP matrix in the form of primary particles, which greatly improved the interfacial interaction between the nanoparticles and the host matrix. The nanoparticles used in this work were surface-modified by coating with fatty acids, which not only enhance the compatibility of filler with the polymer but also

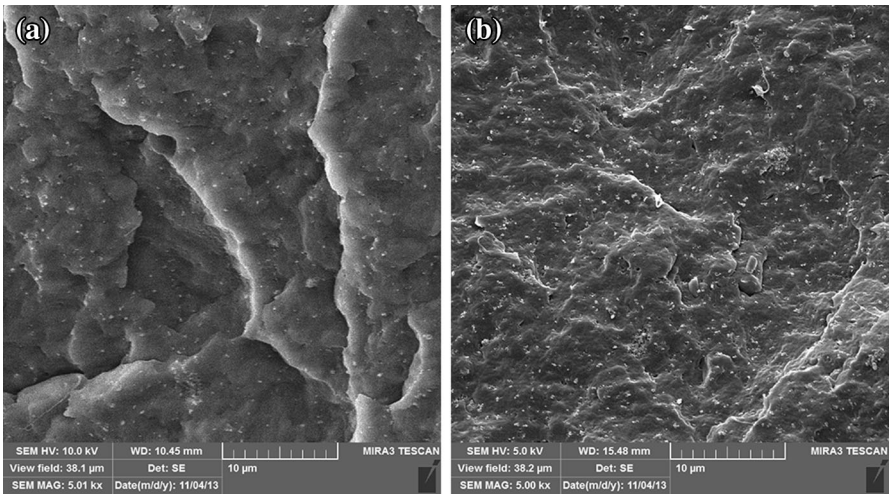

Fig. 1 SEM micrographs of cryo-fractured PP/$CaCO_3$ nanocomposites with different $CaCO_3$ content: **a** 5 wt%, and **b** 10 wt%

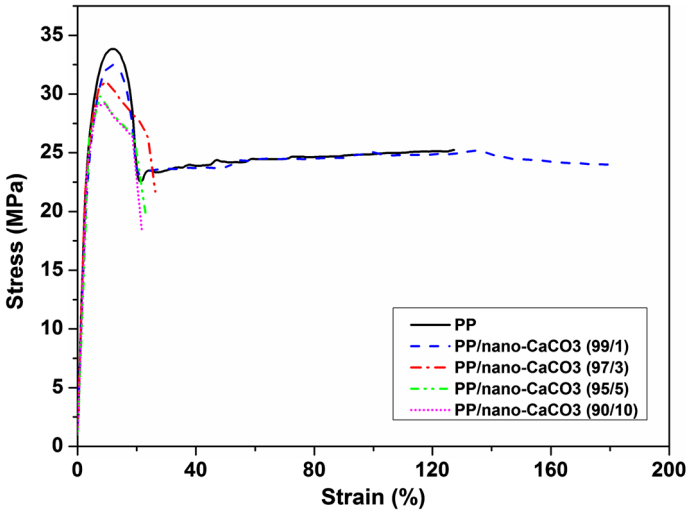

Fig. 2 The typical stress–strain curves of neat PP and PP/$CaCO_3$ nanocomposites of different amounts of $CaCO_3$ nanoparticles

strengthen the interaction between the inorganic filler and polymer. Therefore, the surface treatment of particles plays an important role in the homogeneous dispersion of nanoparticles within the polypropylene matrix for PP/$CaCO_3$ nanocomposites prepared in this work.

The typical stress–strain curves of PP/nano-$CaCO_3$ nanocomposites containing different amounts of nanofiller are represented in Fig. 2. The obtained tensile properties related to each composition are given in Table 2.

Table 2 Tensile properties of neat PP and its nanocomposites (standard deviations in parentheses)

Sample (PP/nano-$CaCO_3$)	Young's modulus (MPa)	Yield stress (MPa)	Strain at break (%)	Ultimate strength (MPa)
100/0	1507 (30)	33.84 (0.3)	127.25 (5)	25.25 (0.6)
99/1	1806 (40)	32.50 (0.4)	179.65 (7)	23.99 (0.6)
97/3	1849 (25)	31.20 (0.6)	26.30 (4)	22.00 (0.5)
95/5	1926 (35)	30.00 (0.4)	23.80 (4)	26.00 (2.0)
90/10	2046 (30)	29.50 (0.3)	21.60 (3)	19.86 (1.2)

The neat PP showed a ductile behavior under the test conditions. The macroscopic deformation behavior of the samples gradually transferred into semi-ductile behavior with $CaCO_3$ nanoparticle contents. As outlined in Table 2, the Young's modulus gradually increased, while the yield stress and ultimate strength decreased with nanofiller concentration. The increase of stiffness with nanofiller content comes from the presence of an inorganic component with much more rigidity and stiffness than the PP matrix. The incorporation of 1 wt% of nano-$CaCO_3$ into PP improved the material extensibility during the tensile testing, as compared with that of neat PP. Further loading of nanofiller, up to 10 wt%, into PP caused a remarked monotonic decrease in the strain at break. The same behavior has been observed by other researchers [1, 7, 23] for PP/$CaCO_3$ composites under the tensile testing. Zhang et al. [23], for instance, found that the addition of 5 and 10 vol% of $CaCO_3$ nanoparticles, with the average particle size of about 44 nm, gradually increased the strain at break of the material compared to the unfilled PP, whereas higher loadings of the nanofiller up to 20 vol% gradually reduced the amount of strain to much lower than that of neat PP. Generally, it is expected that the introduction of rigid filler into a thermoplastic resin reduces the tensile deformability of the resulting material, but in the case of semicrystalline thermoplastics (iPP in this work) it is well documented that the presence of nanofiller may also affect the crystalline morphology of the host matrix. By analyzing the crystalline morphology of PP/$CaCO_3$ nanocomposites of different nanofiller contents, Zhang et al. [23] found that when the nanoparticles were introduced within PP matrix, smaller and imperfect spherulites, compared with those of neat PP, were formed. The reduction of spherulite size and disappearance of sharp interface among spherulites favored the increase in elongation at break for PP/$CaCO_3$ composites. Accordingly, the increased tensile elongation for the nanocomposite containing 1 wt% of nanofiller in the present work can be attributed to the distortion and reduced crystalline texture of the material with the addition of 1 wt% nanofiller. Moreover, it is expected that the Young's modulus, yield stress and tensile strength decrease, and tensile strain increases with the reduction of spherulite size and crystalline structure as a function of nanofiller content. Contrary to this hypothesis, in this work, the Young's modulus increased with filler content and a monotonic decrease in yield stress was not followed by a gradual increase in elongation at break. Therefore, the change in the mechanical properties with nano-$CaCO_3$ content at concentrations higher than 1 wt% is not consistent with the

change in crystalline structure solely. For the composites reinforced by the inorganic fillers, it is well established that the strengthening effect of the filler depends largely on the amount of the interfacial interaction between the filler and the matrix [25]. In the case of poor interfacial interaction, the addition of the rigid particles reduces the yield stress and tensile strength of the resulting material due to the stress concentration effects and early debonding of particles from the matrix [7, 24, 25], while with the strong adhesion at the interfacial region between the phases, the yield stress and ultimate strength will increase as a result of efficient stress transfer from the matrix to the dispersed particles [25]. Although the nanoparticles utilized in the present work were surface treated by fatty acids and exhibited a relatively fine dispersion in the matrix, but the SEM micrographs in Fig. 1b showed that there are a little number of particle aggregates in the microstructure. In addition, it is expected that the number of aggregates increases with particles concentration, because at higher $CaCO_3$ contents the interparticle distance is small, hence flocculation of these nanoparticles could occur during and/or even after the mixing was stopped [24]. Figure 3 displays the SEM micrographs taken from the different zones of necked-down region of specimen for nanocomposite containing 10 wt% of nanofiller fractured under tensile loading. During the tensile loading, the dispersed particles of different sizes act as stress concentrators. At stress levels near the yielding point, the particles debond from the surrounding matrix material, giving rise to the formation of voids at the interfacial regions between the particles and matrix (see Fig. 3a, b). With further loading, the voids would grow and become elongated in the direction parallel to the tensile drawing (see Fig. 3a, b). When the size of the voids approached a critical value, they can serve as precursors for crack nucleation and sites for fast crack propagation, leading to premature fracture of the sample (see Fig. 3c).

As is visible in the micrographs in Fig. 3a, b, the size of voids nucleated around the particles at the interfacial region is closely related to the size of the particles and/or aggregates. The larger the aggregates, the coarser the voids formed at the interface are. This means that the voids generated around the aggregates can easily act as fracture sites rather than those formed around the dispersed domains in the scale of primary particles [7, 24]. In other words, these critical-size voids behaved as the defects in the material, and by formation at the low stress levels as a consequence of early debonding of the coarse aggregates, resulting in a decrease in yield stress, ultimate strength and the deformability of the sample under tensile loading (see Table 2). As a result, the post-yield deformation stability of the material greatly reduced as the number and the size of aggregates increase with nano-$CaCO_3$ content.

It is important to note that Young's modulus is a low-strain property [24, 25]. Obviously, the particles do not debond at these low strains, and therefore the stiffness represented an incremental trend with nanofiller content. The trends of tensile properties as a function of nanofiller content as listed in Table 2 are consistent with the trends reported in the literature for other PP/$CaCO_3$ nanocomposite systems [7, 23, 24].

The effect of $CaCO_3$ nanoparticles on the impact resistance of the PP was evaluated and the results are illustrated in Fig. 4.

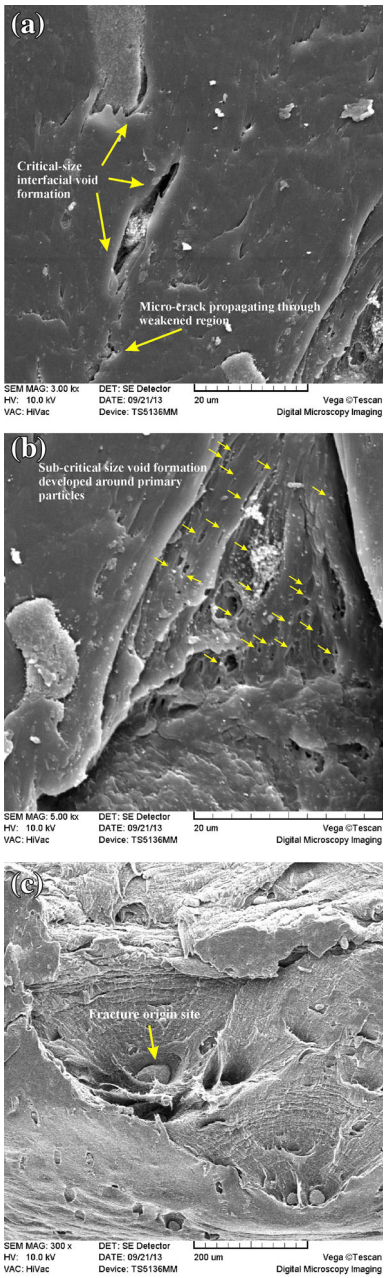

Fig. 3 SEM micrographs taken from the necked-down region of a tensile fractured specimen of PP/$CaCO_3$ (90/10) nanocomposite. **a** Critical-size voids nucleated at the aggregate–matrix interface are elongated in the tensile direction and act as fracture initiation sites, **b** many sub-critical-size cavities formed around primary particles, **c** aggregates of different sizes as fracture origin sites. The tensile deformation was in *vertical* direction

As can be seen in Fig. 4, the impact toughness of the PP progressively improved with the $CaCO_3$ nanoparticles concentration. As is apparent from Fig. 4, the extent of improvement in impact toughness, as compared with that of pure PP, was more than two times. It should be noted that the main reason for using the $CaCO_3$

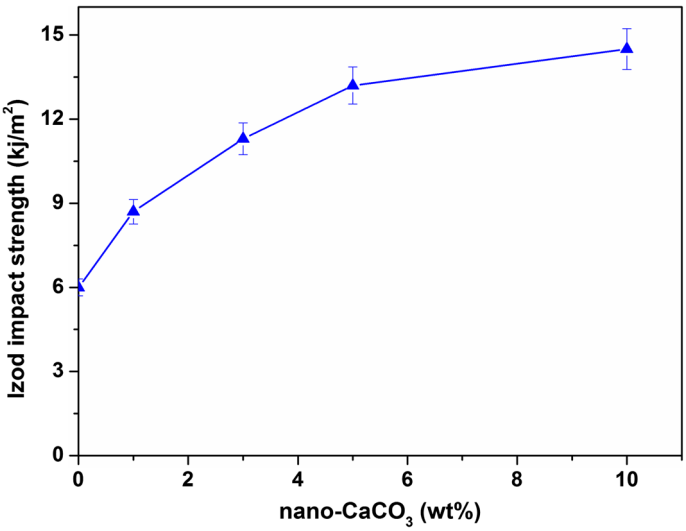

Fig. 4 Notched Izod impact energies of neat PP and PP/$CaCO_3$ nanocomposites of various amounts of $CaCO_3$ nanoparticles

nanoparticles at the present work was to utilize its reinforcing effects as a stiffener, which was approved according to the tensile results. Nevertheless, the tensile and impact results demonstrate that the $CaCO_3$ particles exhibit a dual functionality within PP matrix.

The trend of the notched Izod impact toughness values reported in Fig. 4 is not consistent (with the exception of the sample containing 1 wt% of nanoparticles) with the toughness of various nanocomposites inferred from the stress–strain curves in Fig. 2. As can be seen, the incorporation of nanofiller at concentrations higher than 1 wt% induced larger Izod fracture energies than the unfilled PP, while the same nanocomposites fractured very earlier during the tensile tests. The same differences between the trends of toughness in uniaxial tensile and impact tests have been reported in the literature [7]. Toughness in tensile tests (the area under the stress–strain curves) depends largely on the strain at break, which in turn is governed by the presence of flaws [7]. Izod toughness, on the other hand, is a measure of the energy required for rapid crack propagation. The slow tensile test eventually probes the whole gauge volume of the specimen, whereas Izod test normally only involves the plane directly ahead of the notch tip where, in a material with very low level of plastic response, the fracture becomes unstable. Moreover, the presence of the notch and especially the much higher imposed velocity result in a large value of local strain rate in the Izod experiment, orders of magnitude larger than that in the tensile test [7, 26]. Therefore, it is not surprising that the two toughness measurements present quite different trends.

There are several reports in the literature describing the improved fracture resistance of PP under the impact conditions by the incorporation of $CaCO_3$ micro- and/or nanoparticles [7, 23, 24, 26–29]. The results indicated that the dispersion quality of $CaCO_3$ particles plays a crucial role in toughening efficiency. It is well

established that the formation of aggregates is detrimental for effective toughening [7, 23, 24]. The tendency of particles for aggregation and/or agglomeration largely depends on the size of the particles and their concentration in the system [23, 24]. Agglomeration became worse as the particle size decreased. The improvement in impact strength of the nanocomposites prepared in this work was consistent with the reasonably good state of dispersion of particles in the matrix. SEM micrographs of the cryo-fractured samples of different nanofiller contents in Fig. 1 showed that the particles were dispersed in the matrix predominantly in the form of primary particles, and a little number of aggregates were present in the structure of PP/$CaCO_3$ (90/10) nanocomposites. The formation of small aggregates as a result of an increase in the concentration of $CaCO_3$ nanoparticles from 5 to 10 wt% originates from the lower interparticle distance between the dispersed particles for the system with 10 wt% of nanoparticles which facilitates their collision and subsequent aggregation during the mixing process. According to this, the improved impact resistance of the nanocomposite with 10 wt% of the $CaCO_3$ nanoparticles with respect to the sample containing 5 wt% of nanofiller seems to be in contradiction with the hypothesis that the formation of particle aggregates is detrimental for toughening. However, this enhancement in impact fracture energy could be rationalized by the following reasons. First, the increase in the number of aggregated particles in the nanocomposite containing 10 wt% of nanoparticles is not high enough to induce their severe detrimental effects on the impact fracture toughness (see Fig. 1b); and the second is that the formed aggregates also resist to some extent against the early debonding and subsequent critical-size cavity formation. This latter statement was further confirmed by close examination of the dispersed particles in the matrix via taking SEM micrographs of higher magnification (see Fig. 5).

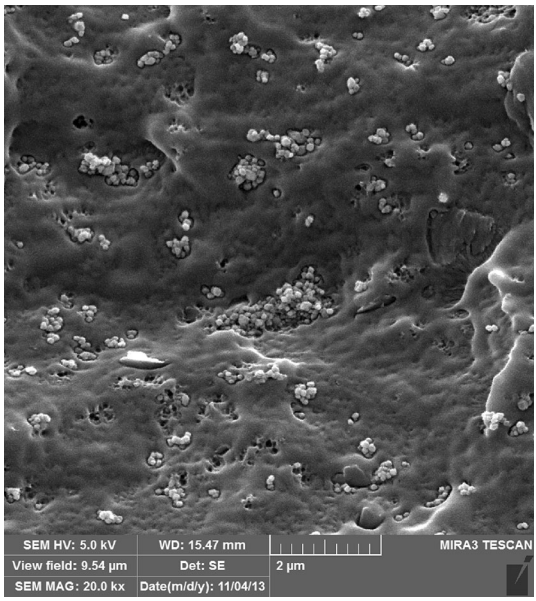

Fig. 5 SEM micrograph of cryo-fractured PP/$CaCO_3$ (90/10) nanocomposite showing particle aggregate embedded within the iPP matrix

From Fig. 5, it is clearly visible that the aggregate of particles is not completely free from the matrix after fast cryogenic fracture of the sample. In turn, they were wetted and sufficiently embedded in the surrounding matrix material. As a result, the impact behavior of the material was not highly affected by the presence of the little number of small aggregates in the microstructure. Also apparent in Fig. 5 is the formation of cavities in the matrix mainly around the dispersed particles due to the debonding of the particles from the surrounding matrix during the cryogenic fracture process. As will be discussed in more detail in the fractographic analysis section, the process of debonding of particles followed by the cavity formation at the interfacial region between the particles and matrix plays a crucial role in stress relief and energy absorption capacity of the surrounding matrix materials during the impact loadings, and consequently improves the fracture toughness.

As stated earlier, in the present work, the ABS was selected as a toughener and its toughening potential for polypropylene was investigated. This impact modifier had a core–shell microstructure in which the polybutadiene core was chemically grafted by poly(styrene-*co*-acrylonitrile) copolymer and, therefore, is extensively used as a toughening agent for styrenic polymers. Its particles size ranged from 0.1 to 1 μm, with the average particle size of about 0.6 μm as reported by supplier. Due to its chemical structure, ABS is not compatible with polypropylene, which adversely affects its efficiency as a toughening agent for polypropylene. Therefore, adequate compatibilization is necessary for achieving a material with good energy absorption capacity [30]. For this reason, the maleic anhydride-grafted polypropylene (PP-*g*-MA) was used as compatibilizer, and the effects of both rubbery phase content and PP-*g*-MA concentration on the phase morphology and mechanical properties of PP/ABS microcomposites (binary systems) were studied. The compatibilizing efficiency of PP-*g*-MA for PP/ABS system is represented in Fig. 6, where the effect of PP-*g*-MA concentration (ranging from 0 to 6 wt%) on the phase morphology of PP/ABS (80/20) blend is illustrated.

In this figure, the holes visible on the cryo-fractured surfaces are corresponded to the location of dispersed ABS particles, which were left after selective solvent etching by tetrahydrofuran. It is believed that the large holes are related to the agglomeration of ABS particles dispersed in the polypropylene matrix, because the size of these domains is much larger than that of primary ABS rubber particles. It can be seen that the incorporation of PP-*g*-MA changes the microstructure of the binary system, in that the size and number of large aggregates presented in the matrix gradually decreased with compatibilizer content. The PP-*g*-MA acted as an emulsifying agent and with preferential localization at the interfacial region increases the interfacial interaction between the ABS particles and the PP matrix, leading to increase of compatibility in the system. As a result, the tendency of dispersed particles for aggregation decreased as the amount of PP-*g*-MA was increased. This finding is in agreement with the results reported in the literature [31, 32]. The change in microstructure, due to improved adhesion at the interfacial region, would affect the macroscopic response of the material under the mechanical tests. The typical stress–strain behaviors of the uncompatibilized and compatibilized PP/ABS (80/20) blends under uniaxial tensile tests are shown in Fig. 7. The effect of PP-*g*-MA concentration on the tensile and impact properties of PP/ABS (80/20)

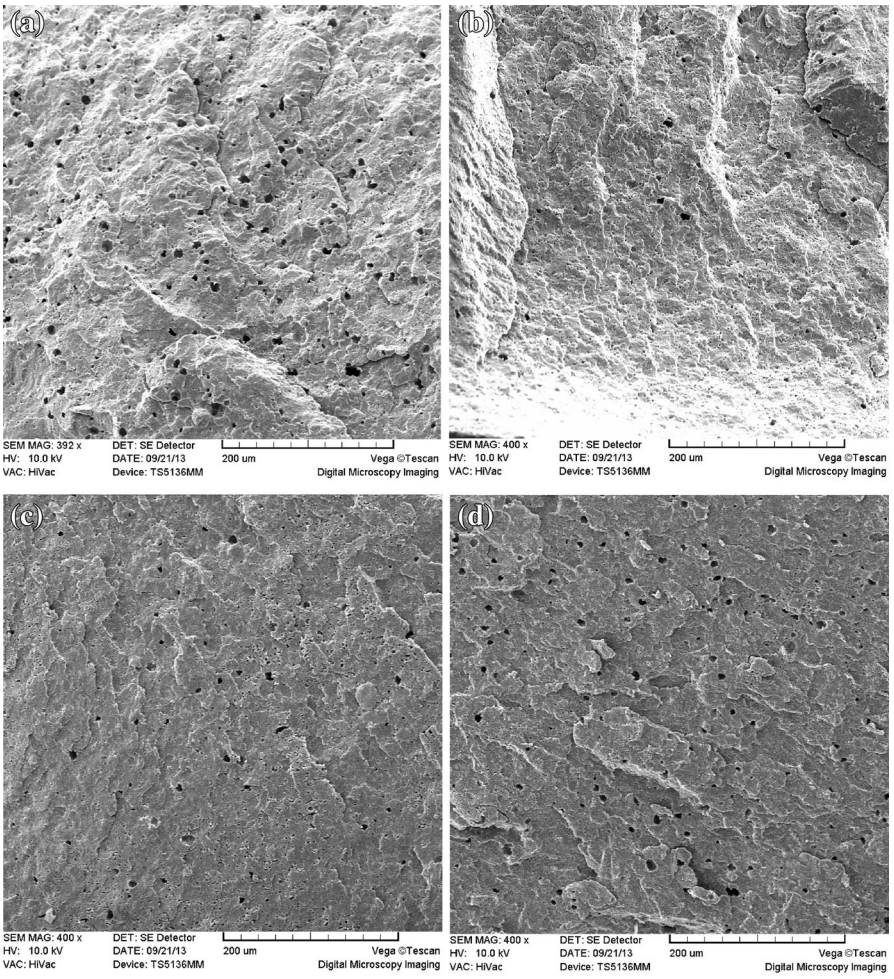

Fig. 6 SEM micrographs taken from cryogenically fractured surfaces of PP/ABS (80/20) blend compatibilized with various amounts of PP-*g*-MA: **a** 0 wt%; **b** 1 wt%; **c** 3 wt%; and **d** 6 wt%. The ABS phase was etched by tetrahydrofuran

blend is listed in Table 3. The addition of PP-*g*-MA resulted in an increase in yield stress, ultimate stress and elongation at break, as compared with those of uncompatibilized blend. The increase in yield stress and tensile strength with compatibilizer content originates from the interfacial activity of PP-*g*-MA, which by localization at the interface region enhances the interfacial interaction between the ABS particles and the matrix and, therefore, prevents the particles from early decohesion from the matrix under tensile tests [32]. The improved interfacial adhesion in the system not only gives rise to a finer dispersion of rubber particles in the matrix, but also causes an efficient stress transfer from the matrix to dispersed

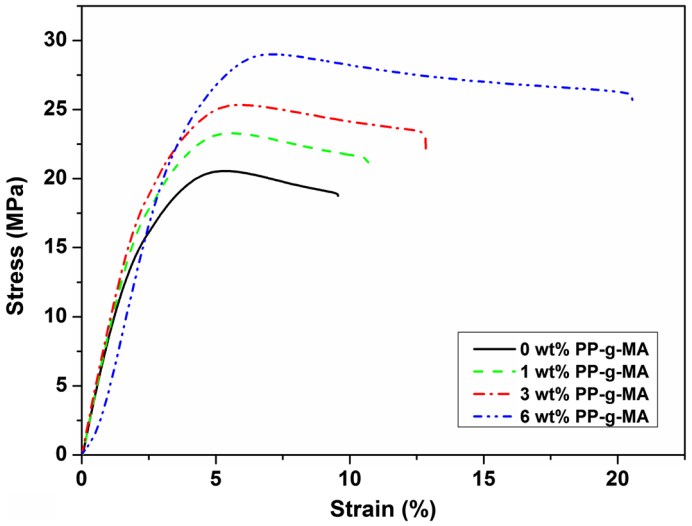

Fig. 7 The typical stress–strain curves of PP/ABS (80/20) blend with different PP-*g*-MA content

Table 3 Mechanical properties of PP/ABS (80/20) blend with different amounts of PP-*g*-MA (standard deviations in parentheses)

Material (PP/ABS/PP-*g*-MA)	Young's modulus (MPa)	Yield stress (MPa)	Strain at break (%)	Tensile strength (MPa)	Izod impact energy (kJ/m^2)
80/20/0	771.70 (20)	20.54 (0.5)	9.50 (4)	18.75 (1.0)	7.40 (1.5)
79/20/1	836.25 (25)	23.30 (1.0)	11.20 (3)	21.16 (0.9)	19.50 (1.0)
77/20/3	871.43 (31)	25.33 (0.8)	12.90 (4)	22.90 (1.1)	20.80 (0.5)
74/20/6	685.70 (35)	29.00 (1.2)	20.55 (6)	25.57 (1.3)	21.20 (1.0)

rubbery particles through the interfacial region. Consequently, the strain at break also increases with compatibilizer content.

The effects of ABS content and compatibilizer concentration on the impact resistance of the PP/ABS blends are displayed in Fig. 8.

The incorporation of 5 wt% of ABS particles into polypropylene slightly increased its impact strength. Further addition of rubber particles to polypropylene at the absence of compatibilizer had no effect on the impact behavior of the material. The introduction of 1 wt% of compatibilizer into PP/ABS blends caused a marked increase in impact toughness. As the concentration of compatibilizer increased to 3 wt%, higher impact properties were obtained. Moreover, for a given amount of compatibilizer, the impact strength gradually increased with percentage of rubbery particles. It is worth to note that the impact resistance of compatibilized PP/ABS/PP-*g*-MA (77/20/3) blend, 20.8 kJ/m^2, was more than three times that of pure polypropylene, 6 kJ/m^2. As reported in Table 3, further addition of PP-*g*-MA (up to 6 wt%) into PP/ABS (80/20) blend caused larger Izod impact energy (21.2 kJ/m^2) due to the higher degree of compatibilization in this system. For this

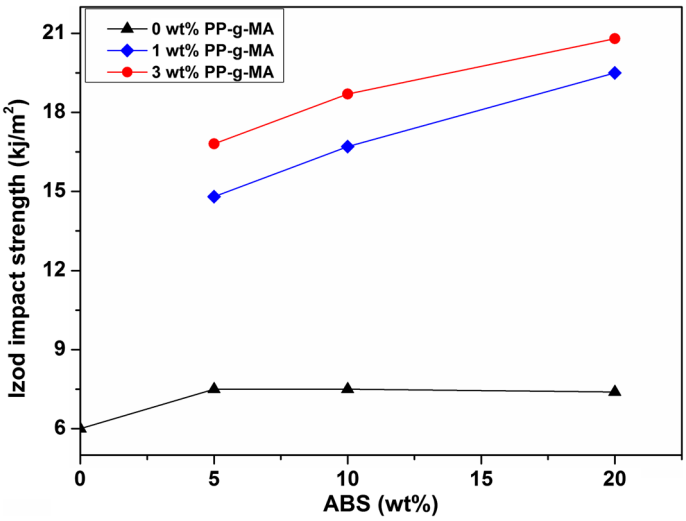

Fig. 8 The effect of PP-*g*-MA concentration on the notched Izod impact energies of PP/ABS blends

composition, the amount of rubber content corresponding to 20 wt% of ABS particles was about 12 wt%. The results of morphological observations and mechanical analysis in this section indicated that in the presence of a suitable compatibilization, ABS could effectively toughen the PP phase.

The results of mechanical analyses conducted on binary systems showed that nano-$CaCO_3$ had a dual functionality in the PP matrix, as both the reinforcing agent and toughener, while ABS mainly enhanced the impact toughness in the presence of a suitable compatibilizing agent with adequate concentration. The phase structure of uncompatibilized and compatibilized PP/ABS/nano-$CaCO_3$ (75/20/5) ternary systems is depicted in Fig. 9. In the case of ternary systems studied in this work, the rubbery particles were etched by the technique similar to that of binary PP/ABS blends. According to Fig. 9, it is believed that the nanofiller particles are distributed in the PP matrix as an isolated phase. In other words, the minor components in the ternary nanocomposite are separately dispersed within the polypropylene matrix.

The two-phase dispersed phase morphology for the ternary composite can be clearly observed in Fig. 9d. It is worth mentioning that for the ternary nanocomposites two main phase morphologies have been reported in the literature [11, 18–20]; one is a morphology with the elastomer and filler particles dispersed independently in the PP matrix. Another has core–shell-type particles consisting of a filler particle core and an elastomer shell. The formation of these morphologies is reported to be strongly dependent on the interactions of the elastomer and filler [18–20]. When no functional group is introduced into the elastomer, the elastomer and the filler particles are dispersed independently in the PP matrix because there is no interaction between the elastomer and the filler particles. On the other hand, when the functionalized elastomer is used to enhance the interaction between the elastomer and filler, the aforementioned core–shell structure could be formed.

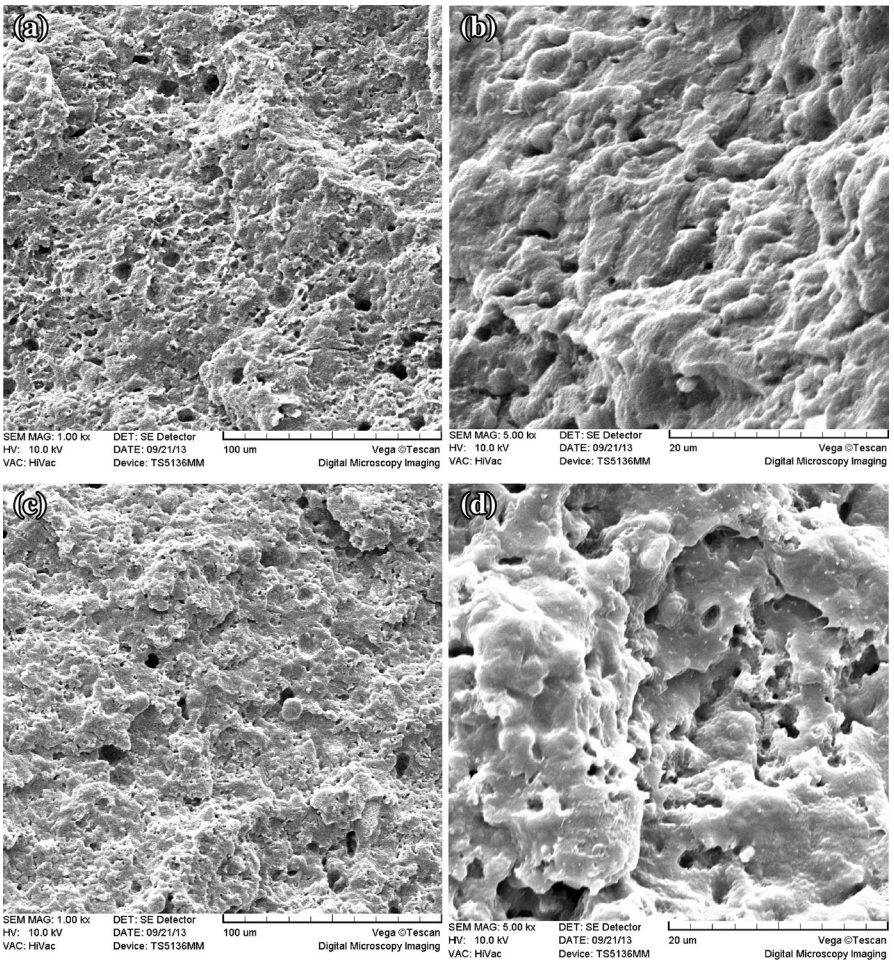

Fig. 9 SEM micrographs with different magnifications taken from cryogenically fractured surfaces of PP/ABS/nano-$CaCO_3$ (75/20/5) ternary system containing different amounts of PP-*g*-MA. **a**, **b** 0 wt%, and **c**, **d** 6 wt%. The ABS phase was etched by tetrahydrofuran

Therefore, the two-phase dispersed morphology found in this work seems reasonable as neither the ABS rubbery phase nor the nanofiller had any functional group in their chemical structure. In addition, the $CaCO_3$ particles were surface treated, which further improves their compatibility with PP and, as a consequence, promotes their isolated distribution within the polypropylene matrix.

The results of Izod impact strength values for PP/ABS/nano-$CaCO_3$ ternary nanocomposites together with some of binary systems are illustrated in Fig. 10.

The data demonstrated that the impact resistance of uncompatibilized PP/ABS/nano-$CaCO_3$ (75/20/5) ternary nanocomposite was slightly larger than that of compatibilized PP/ABS/PP-*g*-MA (74/20/6) binary blend, while a great improvement was obtained as compared with the impact strength value of uncompatibilized

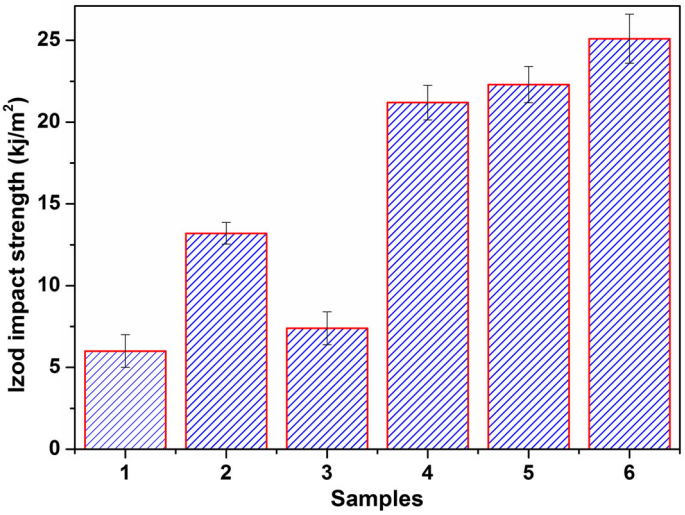

Fig. 10 Comparison of notched Izod impact energies of different samples. *1* PP, *2* PP/$CaCO_3$ (95/5), *3* PP/ABS (80/20), *4* PP/ABS/PP-*g*-MA (74/20/6), *5* PP/ABS/$CaCO_3$ (75/20/5), and *6* PP/ABS/$CaCO_3$/PP-*g*-MA (69/20/5/6)

PP/ABS (80/20) binary blend. This remarked change in impact behavior was ascribed to the deformation micromechanisms and morphological change induced by the introduction of nanofiller into uncompatibilized binary blend. As observed earlier, the addition of 5 wt% of nanofiller into PP increased the impact fracture energy of material. The probable change in phase morphology upon the incorporation of nanoparticles into uncompatibilized PP/ABS blend also may partly contribute to the improved impact energy of the resulting system. The addition of PP-*g*-MA as a compatibilizer further increased the impact toughness of the ternary system. It should be noted that the impact energy value for compatibilized PP/ABS/nano-$CaCO_3$/PP-*g*-MA (69/20/5/6) ternary nanocomposite was more than four times of that of neat PP. This increase in impact fracture toughness is remarkable. The following section describes the fracture surface of the binary and ternary systems studied in this work to elucidate the deformation micromechanisms responsible for each system and their correlations with macroscopic response during the impact loadings.

Fractographic analysis

Study on the morphology of impact-fractured surface is essential to understand the toughening mechanism of PP-based samples. In this work, the characteristics of impact-fractured surfaces were investigated using FEG-SEM instrument. It is well established that the fracture process of the specimen under the impact loading includes at least two steps; crack initiation and crack propagation processes [33, 34]. Thus, to provide more detailed information about the impact fracture process of the

different samples, the overall impact-fractured surfaces were sub-classified as crack initiation zone (zone A), the initial stage of crack propagation (zone B) and the terminal stage of the crack propagation (zone C) as shown in the first image of Fig. 11, according to the analysis utilized by others [35–37].

It should be noted that all fracture surfaces were relatively flat at the macroscopic level and no significant stress-whitening zone was observed (see Fig. 11). The FEG-SEM micrographs with different magnifications taken from the PP and PP-based binary and ternary systems at different zones on the fractured surfaces, as depicted in Fig. 11a, are shown in Figs. 12, 13, 14, 15 and 16. Figure 12 shows the SEM micrographs of neat PP obtained at different regions on the impact-fractured surface corresponding to the different stages of the fracture process. As can be seen, the fracture surface of PP sample at different regions in the direction of crack growth is rather smooth, reflecting the brittle mode of failure with unstable crack propagation [7, 23, 24]. The patterns visible on the fracture surface at the terminal stage of crack propagation (Fig. 12d) are generated by the rapid growth of multiple microcracks through the specimen during the fracture process. The low-magnification micrograph (Fig. 12a) taken at the crack initiation zone shows the fracture initiation point located around 150–200 μm in front of initial notch root. This indicates that a

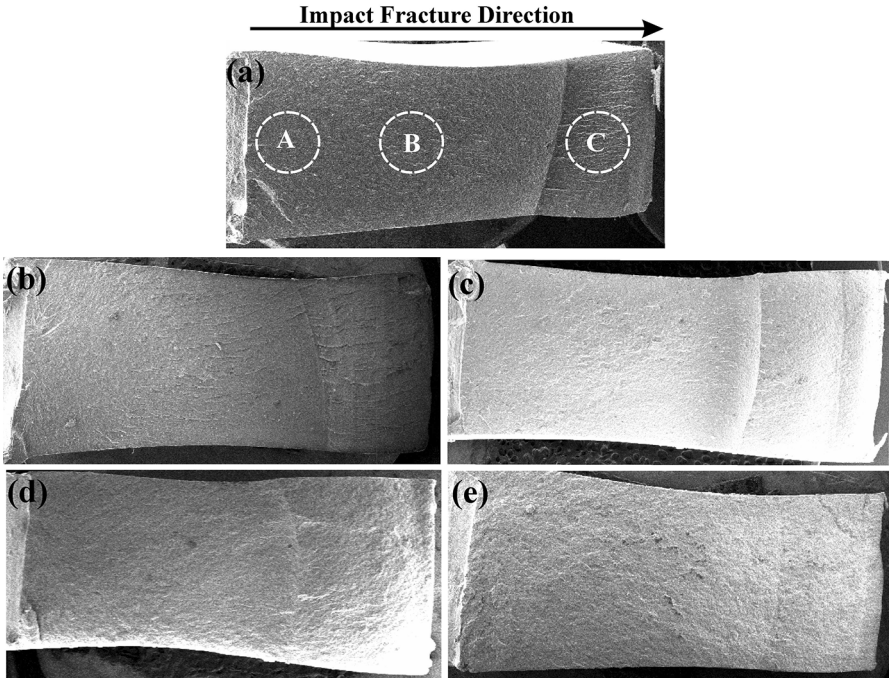

Fig. 11 Low-magnification SEM images showing the impact-fractured surface morphologies of different samples. **a** Pure PP, **b** PP/$CaCO_3$ (95/5) nanocomposite, **c** PP/$CaCO_3$ (90/10) nanocomposite, **d** PP/ABS/PP-*g*-MA (74/20/6), and (**e**) PP/ABS/$CaCO_3$/PP-*g*-MA (69/20/5/6). The regions *A*, *B* and *C* on the first image indicate the crack initiation zone, initial stage of crack propagation and the terminal stage of the crack propagation zones, respectively

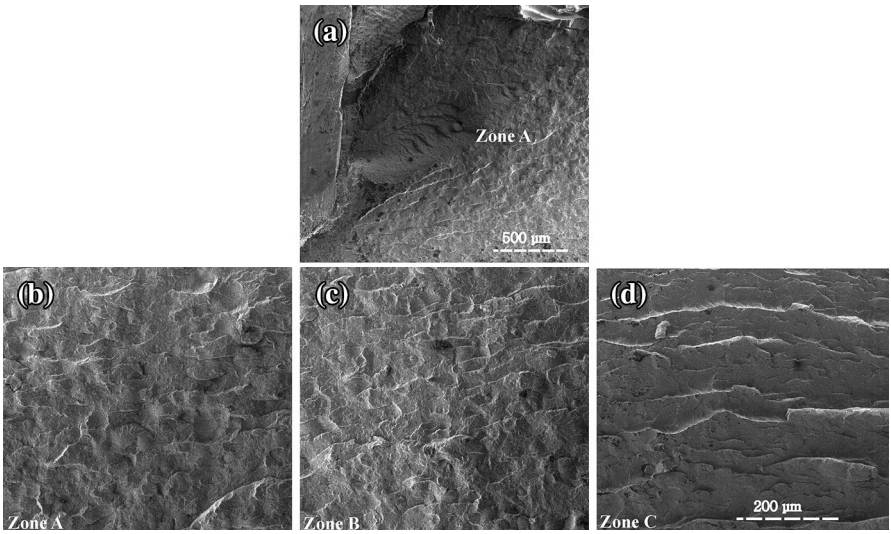

Fig. 12 SEM images showing the impact-fractured surface morphologies of pure iPP sample at different zones. Image **a** at the root of crack tip. Images **b–d** are obtained from zones *A–C* as shown in Fig. 11 at higher magnifications, respectively. The impact fracture direction is from *left* to *right*

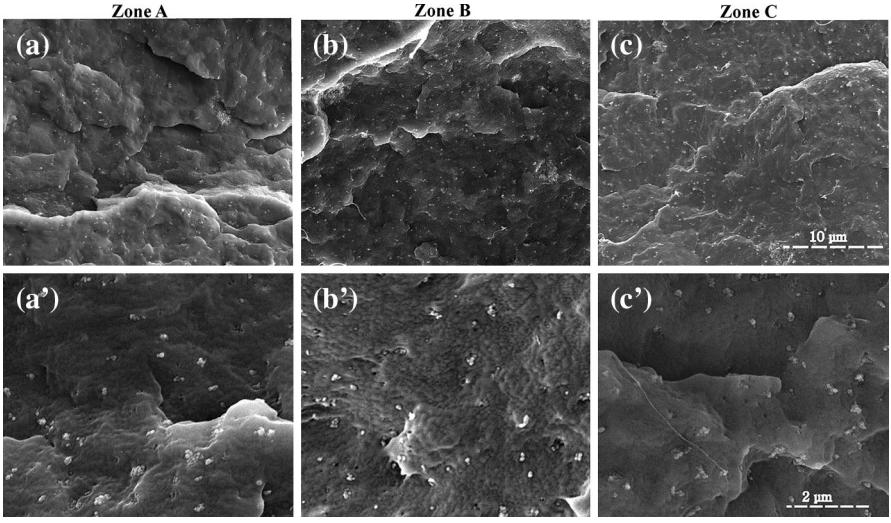

Fig. 13 SEM images showing the impact-fractured surface morphologies of PP/$CaCO_3$ (95/5) nanocomposite obtained from zones *A–C* as shown in Fig. 11 with different magnifications. The impact fracture direction is from *left* to *right*

moderate plastic zone has developed ahead of notch and must have produced a triaxial stress concentration prior to the onset of brittle behavior [7].

Figure 13 shows the textures of impact-fractured surface of PP/$CaCO_3$ (95/5) nanocomposite. This sample showed higher Izod impact energy value than the

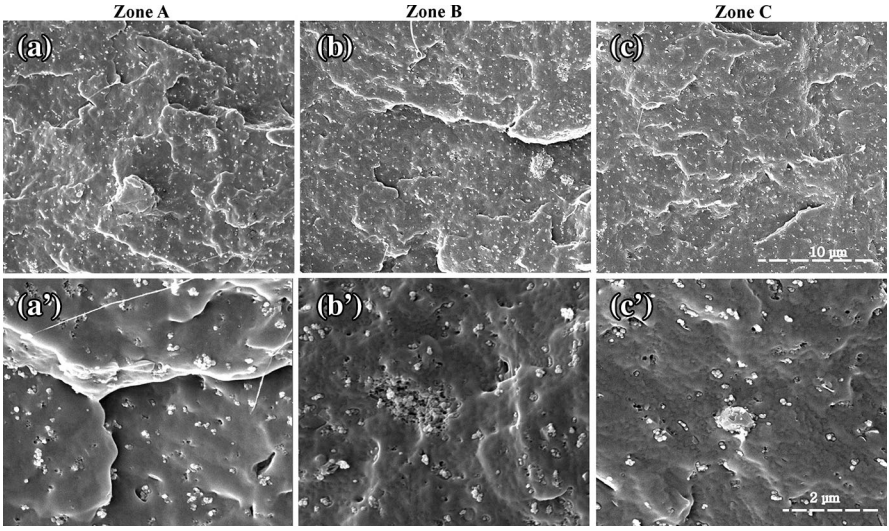

Fig. 14 SEM images showing the impact-fractured surface morphologies of PP/$CaCO_3$ (90/10) nanocomposite obtained from zones *A–C* as shown in Fig. 11 with different magnifications. The impact fracture direction is from *left* to *right*

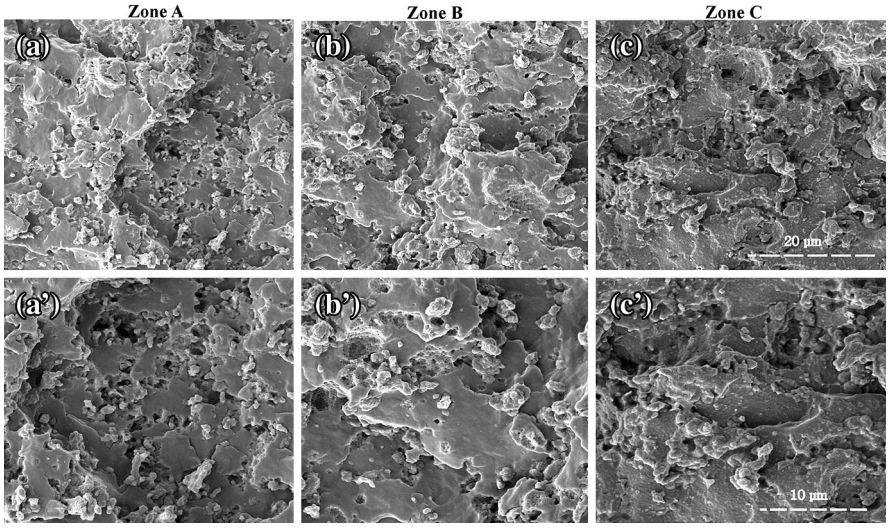

Fig. 15 SEM images showing the impact-fractured surface morphologies of PP/ABS/PP-*g*-MA (74/20/6) blend obtained from zones *A–C* as shown in Fig. 11 with different magnifications. The impact fracture direction is from *left* to *right*

unfilled PP. Since all the samples macroscopically behaved in brittle manner with approximately the same macroscopic fracture patterns, therefore, higher magnification micrographs were taken from the filled binary and ternary samples to get

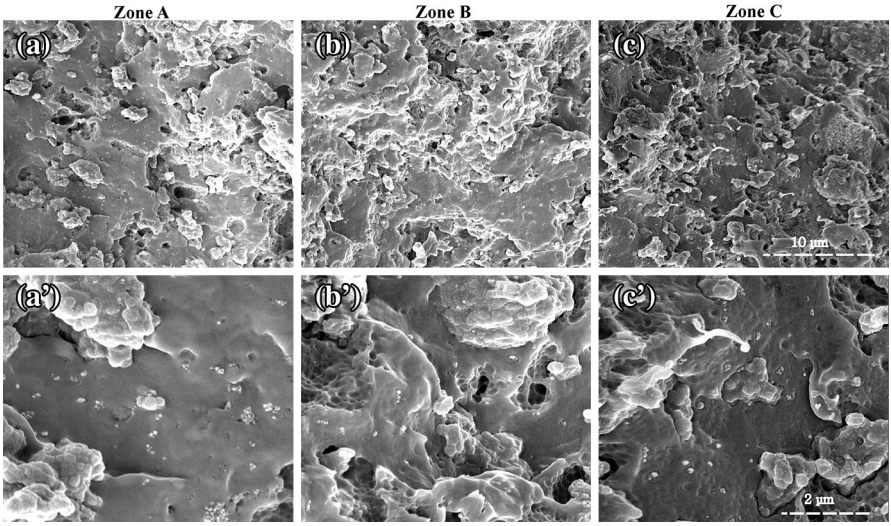

Fig. 16 SEM images showing the impact-fractured surface morphologies of PP/ABS/$CaCO_3$/PP-*g*-MA (69/20/5/6) ternary nanocomposite obtained from zones *A*–*C* as shown in Fig. 11 with different magnifications. The impact fracture direction is from *left* to *right*

more insight into the contribution of different phase in the fracture process, and their corresponding toughening mechanisms under impact loadings.

From Fig. 13a–c, it is apparent that the $CaCO_3$ nanoparticles are uniformly dispersed throughout the PP matrix, although a very little number of aggregates are also visible in these micrographs. In this sample, it seems that the presence of the aggregates had no detrimental effects on the impact fracture behavior of the material. This is because little number of aggregates is formed, and their interfacial interaction with the surrounding matrix seems to be strong enough to prevent them from early decohesion from the matrix and the nucleation of large critical-sized voids. In fact, the low-magnification micrographs display that the cracks propagate through the aggregates rather that their interfaces. With this respect, the aggregates with adequate interaction with the matrix may further increase the energy absorption capacity of the material by crack deflection mechanism [7, 23]. In the SEM micrographs with higher magnification (Fig. 13a′–c′), it is obvious that the nanoparticles are wetted by the matrix material due to their interactions with the PP through fatty acid layer coated on the particles. The surface treatment of the nanoparticles is an essential prerequisite to achieve a homogeneous dispersion in the matrix [7, 23, 24]. Moreover, the formation of stable sub-micron-size cavities in the form of both interfacial voiding at the particle–matrix interface and isolated voiding are clearly visible in the high-magnification micrographs at different zones on the fracture surface. This means that the level of interfacial adhesion is not too strong to prevent the $CaCO_3$ particles from debonding during the impact loadings. This is another condition for rigid particles to act as toughenners. It is well documented that the rigid particles must debond and create free volume in the blend on a sub-micron

size level [23]. This is much like the cavitation mechanism in rubber toughened systems. The voids caused by debonding alter the stress state in the host matrix polymer surrounding the voids [23, 24, 27–29]. This reduces the sensitivity towards crazing since the volume strain is released. The limited shear yielding mechanism becomes operative and the material is able to absorb larger quantities of energy upon fracture [23, 24, 27–29]. Figure 14 exhibits SEM micrographs of the impact-fractured surface of PP/$CaCO_3$ (90/10) nanocomposites at different zones on the fracture surface and in different magnifications. From Fig. 14a–c, it is apparent that at 10 wt% of $CaCO_3$ nanoparticles, the dispersion quality of the nanofiller is still satisfactory although it is expected that the number and the size of aggregates be larger than the nanocomposite with 5 wt% of nano-$CaCO_3$. It is worth noting that the Izod impact strength of PP/$CaCO_3$ (90/10) nanocomposite was higher than that of PP/$CaCO_3$ (95/5). The relatively flat fracture surface of this sample at different zones along the crack propagation direction (Fig. 14a–c) is again representative of brittle fracture behavior.

In the case of the higher magnification micrographs (Fig. 14a′–c′), the fracture surface features are similar to those observed for the PP/$CaCO_3$ (95/5) sample (Fig. 13a′–c′). Many stable sub-micron size voids are developed in the matrix material around the $CaCO_3$ nanoparticles and also as separate cavities as well. As demonstrated above, the interfacial void formation arises from the debonding of nanoparticles from the surrounding matrix in response to stress concentration effects. The isolated cavities generated in the matrix at the space between the particles may be due to either the detachment of nanoparticles from the matrix under the impact loadings or matrix void formation facilitated by the change in the crystalline structure of PP matrix as a result of the presence of $CaCO_3$ nanoparticles. It is important to mention that the stress-whitening phenomenon commonly observed during the deformation of PP under the mechanical tests is mainly due to the formation of numerous voids in the material especially at the amorphous regions between the crystalline layers within the spherulites [38–40]. Therefore, the increase in the number of isolated voids in the material with nano-$CaCO_3$ content may partly be due to a change in the crystalline structure of PP matrix induced by the presence of nanofiller which facilitated the internal void formation in the material under the fracture process. Nevertheless, by considering the shape and the size of the these isolated voids, which are approximately in the same size and shape with the particles and/or small aggregates, it seems that their development be mainly as a result of particles' detachment from the matrix under the impact loadings, leaving sub-micron cavities on the impact-fractured surface. Regardless of the origin and the location of voids in the filled composites, the development of these cavities in a large volume of the material gives rise to a change in the stress state in the surrounding matrix material from triaxial to biaxial or even uniaxial stress, which is more favorable to localized yielding and plastic deformation in the material [7, 23, 24, 27, 29]. Therefore, higher energy is absorbed and/or dissipated during the fracture process and the impact fracture toughness was increased. It should be noted that in nanocomposites with 5 and 10 wt% of $CaCO_3$ nanoparticles as can be seen in the micrographs, the voids formed by debonding and/or detachment of nanoparticles are stable in the sense that they do not coalesce with each other. This is an important

feature of the fracture mechanism; if the cavities grow to a too large size, they could initiate early fracture of the material, resulting in a great reduction in the fracture toughness [7, 24, 25]. The observation of broken down aggregates on the fracture surface in Fig. 14b′ indicates that during the fracture process, the crack propagates through the aggregates rather than their interfaces with the matrix, probably due to the relatively strong interfacial adhesion with the matrix. As stated earlier, the aggregates with adequate interaction with the matrix may further increase the energy absorption capacity of the material by crack deflection mechanism. The observation of voids as a result of debonding of $CaCO_3$ particles and/or domains for binary nanocomposites prepared in this work is consistent with the cavitation mechanism of micro-sized rigid particles as summarized by Gaymans et al. [24], which consists of three stages: stress concentration, debonding and shear yielding. $CaCO_3$ particles served as stress concentrators because of different elastic properties compared to PP. Debonding took place at the $CaCO_3$ particle–PP matrix interface due to an impact load, and voids surrounding $CaCO_3$ particles promoted limited matrix shear yielding. Thus, more fracture work was dissipated and the impact energy improved.

Figure 15 displays the SEM micrographs of fractured surface of compatibilized PP/ABS (80/20) microcomposite taken at various regions on the surface, corresponding to the different stages of crack initiation and crack propagation.

Compared with the samples studied above, the micrographs at different zones of crack initiation and propagation (Fig. 15a–c) show much rougher patterns on the impact-fractured surface of compatibilized PP/ABS (80/20) blend, suggesting higher Izod impact strength value as compared with the pure PP and its nanocomposites containing 5 and 10 wt% of $CaCO_3$ nanoparticles. Although this sample was compatibilized, the morphology of fracture surface at different regions showed some evidences of debonding and/or detachment of ABS particles (phase domains) during the crack initiation and crack propagation stages of the fracture process. There are also some evidences of the localized yielding and plastic deformation of the matrix material surrounding the ABS phase domains in the micrographs of higher magnification (Fig. 15a′–c′). All these deformation processes contribute to higher impact fracture toughness of PP/ABS (80/20) system compared to the PP and PP-based nanocomposites. Similar to rigid $CaCO_3$ nanoparticles described above, the soft ABS microparticles (or domains) in the PP/ABS binary blend also act as stress concentrators, leading to either particles debonding/pull out followed by limited plastic deformation of the surrounding matrix. In some cases, the ABS phase domains were also deformed together with the limited plastic drawing of the matrix material. This is particularly true when an efficient stress transfer from the matrix to the dispersed domains through the interfacial region occurs (Fig. 15c′).

Figure 16 depicts the SEM micrographs of fractured surface of compatibilized PP/ABS/nano-$CaCO_3$ (75/20/5) ternary nanocomposites taken at various regions on the surface corresponding to the different stages of fracture process.

This sample showed the highest Izod impact energy value among the different samples studied in this work. The Izod impact energy for compatibilized PP/ABS/nano-$CaCO_3$ (75/20/5) ternary system was higher than four times that of pure

PP. It seems that the $CaCO_3$ nanoparticles and ABS phase domains have a synergistic effect on the toughening behavior of ternary nanocomposite. The morphology of impact-fractured surface at different zones for this sample was similar to that of compatibilized PP/ABS (80/20) binary blend. The deformation mechanisms operative in the nano-$CaCO_3$-filled nanocomposites elucidated above (Figs. 13, 14) as well as those observed in compatibilized PP/ABS (80/20) blend are the main sources of energy absorption and/or dissipation during the fracture process of compatibilized ternary system, as is visible in the micrographs in Fig. 16. The occurrence of sub-micron-size void formation in the matrix and also around the $CaCO_3$ particles, decohesion and pullout of ABS phase domains along with the plastic deformation of matrix around the rubbery domains in the form of localized fibril formation are clearly seen in the high-magnification micrographs (Fig. 16a′–c′). This is why the impact fracture toughness of ternary nanocomposite is higher than those of binary micro- and nanocomposites. As can be seen in the micrographs, the degree of matrix shear yielding, in the form of localized drawing and fibril formation, around the rubbery domains at the terminal stage of crack propagation (Fig. 16c′) seems to be greater than that of crack initiation (Fig. 16a′) and the onset of crack propagation (Fig. 16b′) zones. This type of deformation behavior was absent at different zones on the fracture surface of binary PP/ABS (80/20) and PP/$CaCO_3$ systems described earlier (see Figs. 13, 14, 15). The micrographs in Fig. 16 also illustrated that the $CaCO_3$ nanoparticles and ABS phase domains were separately distributed in the PP matrix.

Conclusions

Isotactic polypropylene (iPP) was modified by ABS and $CaCO_3$ nanoparticles to enhance the properties of the resulting material. The effect of ABS content and its compatibilization with PP matrix was investigated to evaluate the toughening efficiency of ABS in iPP. The results of morphological and mechanical analyses conducted on the binary PP/ABS blends showed that PP-*g*-MA acts as efficient compatibilizer in the system. The results of Izod impact values demonstrated that ABS could effectively improve the impact toughness of iPP via proper compatibilization. To achieve a simultaneous improvement in stiffness and toughness, the $CaCO_3$ nanoparticles were incorporated into the toughened PP/ABS blend. The mechanical tests performed on binary PP/$CaCO_3$ nanocomposites showed that the introduction of $CaCO_3$ nanoparticles alone into PP matrix not only increases the material stiffness but also enhanced the impact resistance of the material. In the case of ternary nanocomposites, it was observed that the addition of $CaCO_3$ nanoparticles into uncompatibilized PP/ABS blend led to larger Izod impact value as compared with those for corresponding binary compatibilized PP/ABS and PP/$CaCO_3$ systems. Compatibilization further enhanced the impact fracture resistance of ternary PP/ABS/$CaCO_3$ system. Morphological observations revealed separated distribution of minor ABS and $CaCO_3$ components in the PP matrix for ternary systems. The characteristics of impact-fractured surfaces of different binary and ternary samples at different zones on the surface, corresponding to the different

stages of impact fracture process, were closely examined to elucidate the (sub)micromechanisms of deformation operating in different samples. The fractographic results exhibited the development of stable sub-micron-size voids at the nanoparticle–matrix interface and in the matrix in the form of isolated cavities for $CaCO_3$-filled samples, whereas occurrence of debonding and/or detachment of ABS phase domains followed by limited shear yielding of surrounding matrix material in the PP/ABS blends. For compatibilized PP/ABS/$CaCO_3$ (75/20/5) ternary nanocomposite, higher degree of plastic deformation in the form of localized fibril formation at the terminal stage of crack propagation was observed and seems to be responsible for the highest impact energy value among the different samples.

References

1. Rohlmann CO, Failla MD, Quinzani LM (2006) Linear viscoelasticity and structure of polypropylene–montmorillonite nanocomposites. Polymer 47(22):7795–7804
2. Pérez E, Alvarez V, Pérez CJ, Bernal C (2013) A comparative study of the effect of different rigid fillers on the fracture and failure behavior of polypropylene based composites. Compos Part-B 52:72–83
3. Hammani S, Moulai-Mostefa N, Benyahia L, Tassin JF (2012) Effects of composition and extrusion parameters on the morphological development and rheological properties of PP/PC blends. Co-continuity investigation. J Polym Res 19:9940
4. Su F, Huang H, Zhao Y (2011) Microstructure and mechanical properties of polypropylene/poly(-ethylene-*co*-octene copolymer)/clay ternary nanocomposites prepared by melt blending using supercritical carbon dioxide as a processing aid. Compos Part B-Eng 42(3):421–428
5. Kiss A, Fekete E, Pukánszky B (2007) Aggregation of CaCO3 particles in PP composites: effect of surface coating. Compos Sci Technol 67(7–8):1574–1583
6. Yang H, Zhang Q, Guo M, Wang C, Du R, Fu Q (2006) Study on the phase structures and toughening mechanism in PP/EPDM/SiO_2 ternary composites. Polymer 47(6):2106–2115
7. Thio YS, Argon AS, Cohen RE, Weinberg M (2002) Toughening of isotactic polypropylene with $CaCO_3$ particles. Polymer 43(13):3661–3674
8. Ma Y, Wu D, Liu Y, Li X, Qiao H, Yu ZZ (2014) Electrically conductive and super-tough polypropylene/carbon nanotube nanocomposites prepared by melt compounding. Compos Part B 56:384–391
9. Tiwari R, Paul DR (2011) Polypropylene–elastomer (TPO) nanocomposites: 2. Room temperature Izod impact strength and tensile properties. Polymer 52(24):5595–5605
10. Yang H, Zhang X, Qu C, Li B, Zhang L, Zhang Q, Fu Q (2007) Largely improved toughness of PP/EPDM blends by adding nano-SiO_2 particles. Polymer 48(3):860–869
11. Hikasa S, Nagata K, Miyahara K, Izumi T, Suda T, Toyohara A, Kato A, Nakamura Y (2009) Influence of the incorporation of fine calcium carbonate particles on the impact strength of polypropylene/polystyrene-block-poly(ethylene butene)-block-polystyrene blends. J Appl Polym Sci 114(2):919–927
12. Wang X, Xu KJ, Xu XB, Park SJ, Kim S (2009) Selective particle distribution and mechanical properties of nano-$CaCO_3$/ethylene–propylene–diene terpolymer/polypropylene composites with high content of nano-$CaCO_3$. J Appl Polym Sci 113(4):2485–2491
13. Gong L, Yin B, Li LP, Yang M-B (2011) The effects of different processing methods on the morphology and properties of PP/EPDM/Nano-$CaCO_3$ ternary blend. J Macromol Sci B Phys 50(4):806–820
14. Gong L, Yin B, Li LP, Yang M-B (2012) Morphology and properties of PP/EPDM binary blends and PP/EPDM/nano-$CaCO_3$ ternary blends. J Appl Polym Sci 123(1):510–519
15. Gong L, Yin B, Li LP, Yang M-B, Xie B-H, Feng J-M (2013) The morphology and mechanical properties of PP/EPDM/nano-CaCO3 composites: effect of initial mixing state. Polym Bull 70(11):2935–2952

16. Guo HF, Packirisamy S, Gvozdic NV, Meier DJ (1997) Prediction and manipulation of the phase morphologies of multiphase polymer blends: 1. Ternary systems. Polymer 38(4):785–794
17. Dasari A, Yu ZZ, Mai YW (2005) Effect of blending sequence on microstructure of ternary nanocomposites. Polymer 46(16):5986–5991
18. Long Y, Shanks RA (1996) PP–elastomer–filler hybrids. I. Processing, microstructure, and mechanical properties. J Appl Polym Sci 61(11):1877–1885
19. Long Y, Shanks RA (1996) PP/elastomer/filler hybrids. II. Morphologies and fracture. J Appl Polym Sci 62(4):639–646
20. Li Z, Guo S, Song W, Hou B (2003) Effect of interfacial interaction on morphology and mechanical properties of PP/POE/BaSO4 ternary composites. J Mater Sci 38(8):1793–1802
21. Ma C-G, Mai Y-L, Rong M-Z, Ruan W-H, Zhang M-Q (2007) Phase structure and mechanical properties of ternary polypropylene/elastomer/nano-CaCO3 composites. Compos Sci Technol 67(14):2997–3005
22. Qian J, Cheng G, Zhang H, Xu Y (2011) Preparation and characterization of polypropylene/silica nanocomposites by gamma irradiation via ultrafine blend. J Polym Res 18(3):409–417
23. Zhang QX, Yu ZZ, Xie XL, Mai YW (2004) Crystallization and impact energy of polypropylene/CaCO 3 nanocomposites with nonionic modifier. Polymer 45(17):5985–5994
24. Zuiderduin WCJ, Westzaan C, Huetink J, Gaymans RJ (2003) Toughening of polypropylene with calcium carbonate particles. Polymer 44(1):261–275
25. Fu YSY, Feng XQ, Lauke B, Mai YW (2008) Effects of particle size, particle/matrix interface adhesion and particle loading on mechanical properties of particulate–polymer composites. Compos Part B-Eng 39(6):933–961
26. Chan CM, Wu J, Li JX, Cheung YK (2002) Polypropylene/calcium carbonate nanocomposites. Polymer 43(10):2981–2992
27. Lin Y, Chen H, Chan CM, Wu J (2010) The toughening mechanism of polypropylene/calcium carbonate nanocomposites. Polymer 51(14):3277–3284
28. Dasari A, Zhang QX, Yu ZZ, Mai YW (2010) Toughening polypropylene and its nanocomposites with submicrometer voids. Macromolecules 43(13):5734–5739
29. Lin Y, Chen H, Chan C-M, Wu J (2011) Effects of coating amount and particle concentration on the impact toughness of polypropylene/CaCO3 nanocomposites. Eur Polym J 47(3):294–304
30. Bucknall CB (1977) Toughened plastics. Applied Science, London
31. Kum CK, Sung YT, Kim YS, Lee HG, Kim WN, Lee HS, Yoon HG (2007) Effects of compatibilizer on mechanical, morphological, and rheological properties of polypropylene/poly (acrylonitrile-butadiene-styrene) blends. Macromol Res 15:308
32. Lee HG, Sung YT, Lee YK, Kim WN, Yoon HG, Lee HS (2009) Effects of PP-g-MAH on the mechanical, morphological and rheological properties of polypropylene and poly (acrylonitrile-butadiene-styrene) blends. Macromol Res 17(6):417–423
33. Tanniru M, Yuan Q, Misra RDK (2006) On significant retention of impact strength in clay–reinforced high-density polyethylene (HDPE) nanocomposites. Polymer 47(6):2133–2146
34. Yuan Q, Misra RDK (2006) Impact fracture behavior of clay–reinforced polypropylene nanocomposites.. Polymer 47(12):4421–4433
35. Bai H, Wang Y, Song B, Huang T, Han L (2009) Effects of nucleating agents on microstructure and fracture toughness of poly(propylene)/ethylene–propylene–diene terpolymer blends. J Polym Sci Part B Polym Phys 47(1):46–59
36. Yang G, Han L, Ding H, Wu H, Huang T, Li X, Wang Y (2011) Fracture resistance improvement of polypropylene by joint action of core–shell particles and nucleating agent. Mater Sci Eng A 528(3):1382–1390
37. Wu H, Li X, Chen J, Shao L, Huang T, Shi Y, Wang Y (2013) Reinforcement and toughening of polypropylene/organic montmorillonite nanocomposite using β-nucleating agent and annealing. Compos Part B-Eng 44(1):439–445
38. Pawlak A, Galeski A (2005) Plastic deformation of crystalline polymers: the role of cavitation and crystal plasticity.. Macromolecules 38(23):9688–9697
39. Pawlak A (2007) Cavitation during tensile deformation of high-density polyethylene. Polymer 48(5):1397–1409
40. Pawlak A, Galeski A (2008) Cavitation during tensile deformation of polypropylene. Macromolecules 41(8):2839–2851